In-situ characterization of strain in lithium battery working electrodes

Jubin Chen [a],[*], Arjun K. Thapa [b], Thomas A. Berfield [a]

[a] *Department of Mechanical Engineering, University of Louisville, Louisville, KY 40292, United States*
[b] *Conn Center for Renewable Energy Research, University of Louisville, Louisville, KY 40292, United States*

HIGHLIGHTS

- We investigate relationship between electrode capacity and mechanical deformation.
- *In-situ* monitoring of the working electrode surface is performed.
- Digital image correlation is used to quantify electrode strains.
- The effect of constraint due to substrate stiffness is examined.

ARTICLE INFO

ABSTRACT

During lithiation and detlithiation, substantial volumetric changes occur within the electrode materials used for rechargeable lithium batteries. The magnitude of these deformations is inherently linked to the electrical capacity of the battery electrical capacity, which tends to degrade with repeated cycling. In this work, the relationship between electrical discharge capacity and mechanical deformation state is examined using *in-situ* imaging of the working electrode surface within a custom CR2032 coin cell lithium battery. Digital image correlation is used to quantify electrode strains throughout the discharge –charge process. The effect of constraint due to substrate stiffness is investigated for two film materials: traditional graphite and a carbon nanotube based composite. Results for all cases show that as discharge capacity decreases with repeated cycling, increasing residual electrode strains are observed. The thin, compliant foil substrates allowed over double the bi-axial strain state to be induced within electrodes, compared to that found for the thick copper disk substrates under the same electrical cycling conditions.

1. Introduction

The rapid upsurge in mobile consumer electronics device usage has in large part fueled the current substantial demand for high performance rechargeable lithium ion batteries. Due to their outstanding capacity-to-weight ratios, low charge loss rates, and minimal hysteresis effects, lithium ion batteries have become the dominant power storage choice for applications across multiple industrial and consumer sectors. Future advances in lithium ion battery performance will likely come from new material developments and optimization of the coupled chemical, electrical, and mechanical interactions that take place within these rechargeable power storage units. Selection of the anode material is one of the key considerations affecting lithium ion battery capacity

and performance degradation, as these issues are intrinsically related to break-down mechanisms occurring at the material microstructure level.

Graphite has served as the standard anode choice for the first generations of mass produced lithium ion batteries, primarily due to its cost effectiveness. Some of the major limitations of graphite include its relatively low specific capacity (only 372 mAh g^{-1}) [1], and substantial irreversible capacity losses during the initial discharge–charge cycles [2–5]. A major source of irreversible capacity loss is the formation of a solid electrolyte interface (SEI) film on the anode surface, the prevalence of which is directly related to the Brunauer–Emmett–Teller (BET) surface area and anode material density [3–8].

Alternative materials to carbon-based anodes offer enticing theoretical specific capacities, including silicon (4200 mAh g^{-1}), tin (994 mAh g^{-1}), magnesium (3350 mAh g^{-1}), Li$_4$Ti$_5$O$_{12}$ (mAh g^{-1}) and others [9]. The downside to higher specific capacity materials is the generally larger volumetric change induced during lithiation/

delithiation cycles. Such deformations can induce damage modes that can drastically shorten the overall battery service lifetime such as delamination from the current collector or cracking within the anode material [10–17].

One coping mechanism is to use nanoscale-sized particulate forms of these materials in composite anodes. The large volumetric expansions are focused within the nanoscale structures, which are surrounded by binder materials that are typically more compliant. The reduced constraint conditions can help to limit mechanical damage within the intercalated material. Zhang et al., demonstrated that nanowires made with carbon, aluminum or copper coatings significantly reduced radial expansion and tensile stresses, in addition to improving electronic conduction [18]. Numerous examples of this general strategy have been reported, including use of nanostructured forms of silicon [19,20]. However, silicon-based nanoscale particulate (nanowires, nanospheres, etc.) have been shown susceptible to intercalation cracking over a range of dimensional feature sizes [21–23] due to the extremely large volume changes and stress gradients within individual structures caused by lithiation fronts.

The use of nanoscale carbon-based particulate for anodes has also been explored, with highly encouraging results. In particular, carbon nanotubes (CNTs) have been widely used for lithium ion battery electrodes, with recent studies showing that CNT-based anodes can provide high electrical capacity, while reducing anode pulverization due to cycling dramatically [24]. Additionally, aligned carbon nanotube anodes have demonstrated limited capacity degradation after upwards of 50 discharge–charge cycles [25]. The effects of different carbon nanostructure morphologies (single wall, double wall, and multi-wall carbon nanotube configurations) have also been investigated [26], showing the influence of surface area on SEI film growth and capacity degradation. Hybrid combinations of these materials have also been attempted [27] using carbon nanotube infused silicon composite films as anodes.

Quantifying the mechanical deformations associated with lithiation/delithiation is critical for optimal battery performance and lifetime design, but direct measurement of electrode mechanical deformations that accompany electrical cycling of lithium ion battery systems is challenging. Nearly all other previous studies attempting to measure *in-situ* electrode deformations have employed optically-based methods for observing the electrode inside a custom battery arrangement. Sethuraman et al., [28,29] analyzed a silicon thin film system by using a laser optical detection method to determine *in situ* stress and mechanical property changes during discharging/charging. *In-situ* mechanical stress evaluation for Ni–Sn alloy anodes was performed by Chen et al., [11] using another laser measurement technique. In a similar way, Qi and Harris [30] used a custom battery fixture to observe deformation and cracking of a graphite electrode. In that study, the graphite deformation was determined using digital image correlation (DIC). Other uses of DIC includes a recent study by E.M.C. Jones et al., [31] in which lithium ion battery composite electrodes were investigated.

One important issue not addressed by many of these previous works is the role of the mechanical constraint on the anode material, specifically the current collecting substrate. In this work, the effect of substrate stiffness is investigated with respect to the residual strain development and capacity degradation that accompany electrical cycling of lithium ion batteries. Two battery electrode materials are studied, a traditional graphite system and a carbon nanotube-based variation. In both cases, a custom coin cell configuration is used to facilitate *in-situ* strain measurements optically by the digital image correlation method. Both the first-cycle and repeated cycling strain effects are explored.

2. Experimental

2.1. Materials and sample preparation

Lithium batteries were fabricated based on a modification of the standard CR2032 coin cell configuration. The custom variation of this battery cell enables optical imaging of the working electrode throughout the process of battery cycling. Graphite-based thick films (10 μm) deposited on copper substrates were used as the working electrode within the custom coin cell batteries. To investigate the effects of substrate constraint, two types of copper substrates were tested, 16 μm thick copper foils and 635 μm copper disks. While thick copper current collectors may be cost prohibitive for some commercial applications, the 635 μm copper disks used in this work allowed for direct testing of substrate stiffness influence in a controlled manner by varying only one parameter. In practice, the stiffness of a substrate may be controlled in a variety of other, more cost-effective manners to obtain optimal battery performance. In addition, the effects of using conductive carbon nanotubes (CNTs) as graphite replacement were studied.

Graphite electrodes were prepared by mixing 80 wt% graphite powder, 10 wt% carbon black, and 10 wt% polyvinylidene fluoride (PVDF) binders in N-Methyl-2-pyrrolidone (NMP) solvent. The well-mixed slurry was deposited over the copper substrate, and a film casting doctor blade apparatus was used to skim the wet electrode to a thickness of 10 microns. The electrodes and substrates were then immediately put into a laboratory oven at 115 °C for 15 min.

Specimens containing the conductive CNTs as a graphite replacement were prepared in a similar manner. The CNTs used in this study were purchased in bulk commercially (Cheaptubes.com) and had diameters in a range of 60–80 nm and lengths in the range of 10–15 μm. The 80 wt% CNTs were first combined with 10 wt% carbon black and blended in an industrial mixer a period of 12 h. Next, 10 wt% PVDF binder and NMP solvents were injected into the mixture, which was then blended for an additional 12 h. The slurry was then cast onto the copper substrates, skimmed to the proper thickness, and finally oven cured at 115 °C for 15 min.

To allow optical access to the working electrode, a 6.35 mm diameter through-hole was first placed through the center of the coin cell cover cap using a mechanical punch. A 12 mm diameter round, 0.15 mm thick glass cover slip (Ted Pella) was bonded to the top surface of the cell cap by applying CRL 349 ultraviolet adhesive (Loctite Impruv), followed by a 2 min UV exposure cure. This top cover was found to be sufficient to seal the coin cell, but necessitated a custom fixture during crimping to prevent damage to the glass window.

The custom CR2032 coin cell was assembled in an Argon filled glove box. All parts, including cell cap, gasket, spring (Hohsen), and glass fiber separator (Advantec) were put into a 80 °C heated chamber (Buchi glass oven B585) and connected to a vacuum pump for 8 h to completely remove water moisture and evaporated solvent prior to assembly. For all coin cell configurations, a pure lithium metal disk (Sigma Aldrich) was used as the counter electrode. Additional through-holes, approximately 6 mm in diameter, were created in both the lithium metal disk and the separator while housed under the assembly glove box using a gasket punch.

An electrolyte consisting of 1 M LiPF6-EC:DMC (1:2 by volume) was used throughout this work, with ca. 0.5 mL volume used for each cell. After stacking the layers and adding the electrolyte, a hand-operated crimping tool (Hohsen) was used to close and seal the coin cell batteries. A schematic showing the individual coin cell layers and an actual completed coin cell after assembly are shown in Fig. 1.
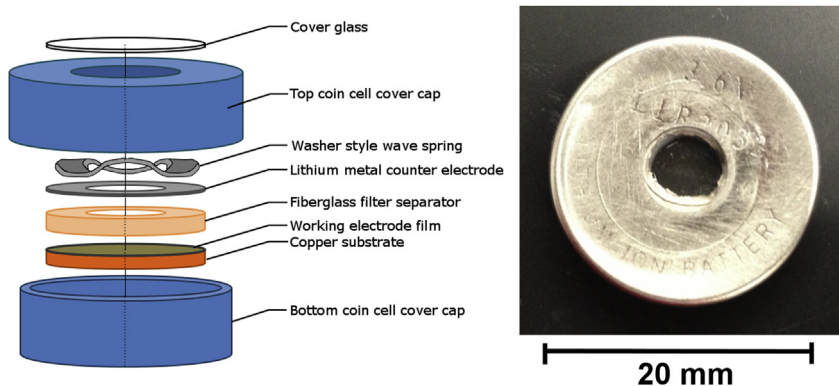
Fig. 1. Coin cell structure diagram (left) and a typical actual coin cell (right).

In addition to the operational batteries tested in this work, identically prepared electrode film/substrate combinations were fabricated for residual strain characterization. The backsides of the substrates for these specimens were mounted with strain gages (CEA-06-062UT-350, Micro-Measurements) prior to electrode film deposition. After curing (115 °C for 15 min) and cooling to room temperature, the substrate residual strains were measured and used to quantify the initial strain levels within the electrode films.

2.2. Testing conditions

Electrochemical performance characterization of the custom CR-2032 coin-type cells was conducted in an Arbin BT2000 battery tester. Immediately after fabrication, the coin cell batteries were electrically cycled while the images were simultaneously taken of the electrode surface. Batteries were first discharged under 0.1 mA constant current conditions until a cut-off voltage of 0.020 V was reached. After a 30 s rest period, a constant current of 0.1 mA was applied to cell during the charging cycles until the battery high potential cut-off was reached, which was 3 V for the graphite electrode and 2 V for the CNT electrode systems. After a 30 s rest period, a 3 V constant voltage charge for graphite or a 2 V constant voltage charge for CNT anode systems was applied to the battery for 5 s. After a 10 s cool down, the next discharge cycle was begun. This process was repeated for approximately 20 cycles using the same loading conditions.

Prior to beginning the first electrical cycle, a reference image of the electrode surface "as fabricated" in the sealed custom coin cell was taken which served as the baseline state for later deformation measurements during electrical cycling. Typical optical images of the electrode surfaces are shown in Fig. 2(a) and (b), while the microstructures of both surfaces are shown in SEM images in Fig. 2(c) and (d).
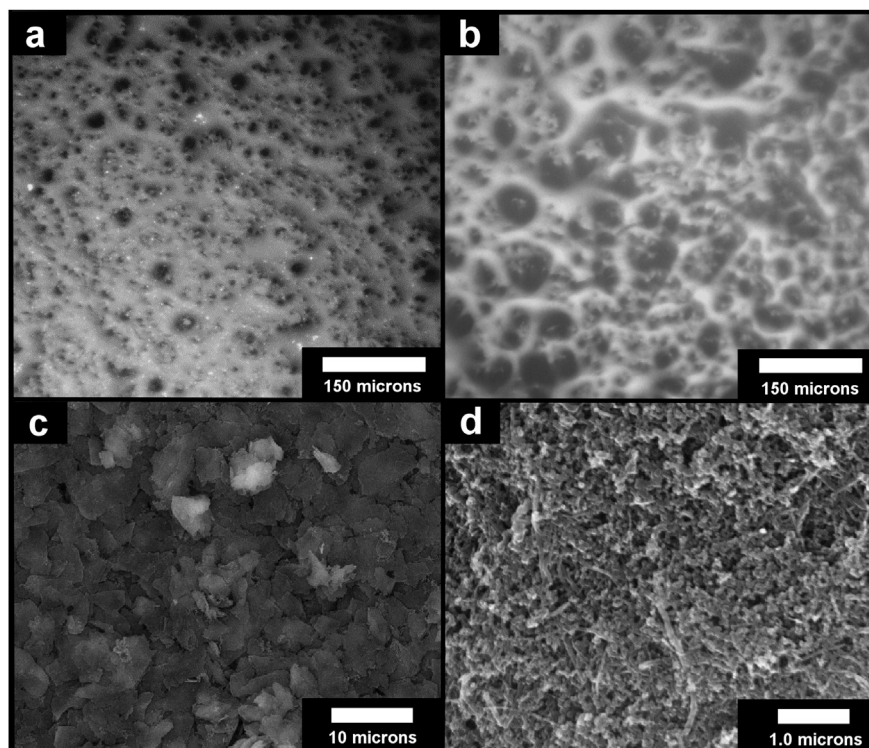

Fig. 2. Optical microscope images of a typical graphite electrode surface (a) and CNT-based electrode surface (b) and SEM images of graphite (c) and CNT surface (d).
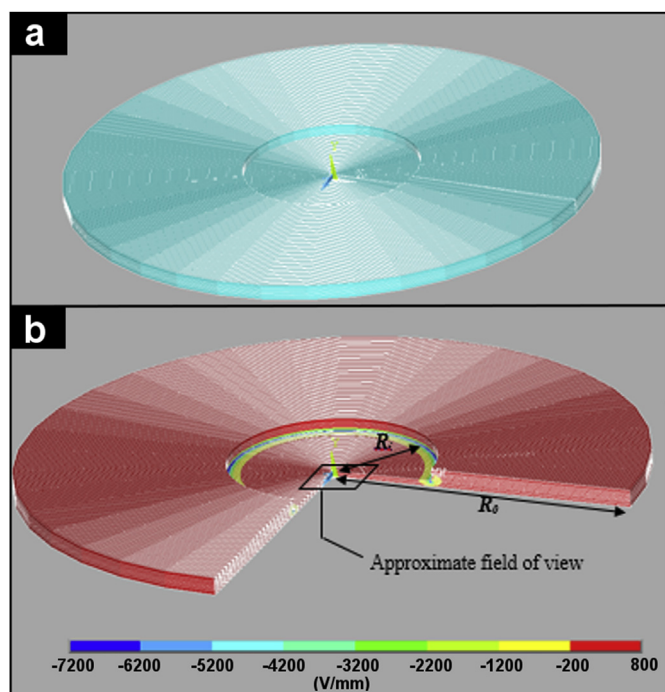
Fig. 3. Finite element model mesh of the full plate bottom working electrode and the top lithium metal counter electrode with center hole removed (a), and the ANSYS simulated electrical field generated between them for a 3 V applied potential differential (b).

Optical microscope images of the electrode surface in the custom coin cell configuration were taken using a Leica DMR microscope mounted with a Retiga 4000R digital camera (2048 × 2048 pixels; QImaging) and a 10× long working distance objective lens. For digital image correlation analysis, the images obtained had a full field of view of 1 mm × 1 mm. Calibration tests were used to estimate the displacement measurement resolution of the optical system under these conditions.

During electrical performance testing, a series of images were taken throughout the initial 4–5 cycles. Beyond the 5th cycle, images were only taken at the fully charged and fully discharged states. These images of the electrode surface during the lithiation/delithiation process were then analyzed using a DIC algorithm with respect to the initial reference deformation state.

2.3. Digital image correlation analysis

Developed originally in the 1980s by Sutton and his colleagues [32–34], digital image correlation (DIC) uses numerical algorithms performed on optically recorded images taken of a specimen surface during an applied loading. The outputs of a DIC experiment are the surface displacements and strains over the full imaged field (in-plane for 2D versions). Given the difficulties presented by the experimental measurements of electrode strain development, DIC offers several advantageous aspects. Some of these benefits include providing full-field displacement measurements and a non-contact measurement, allowing for a wide range of potential specimen dimensions.

The inherent surface roughness of the substrate was found to provide a suitable pattern for performing digital image correlation.
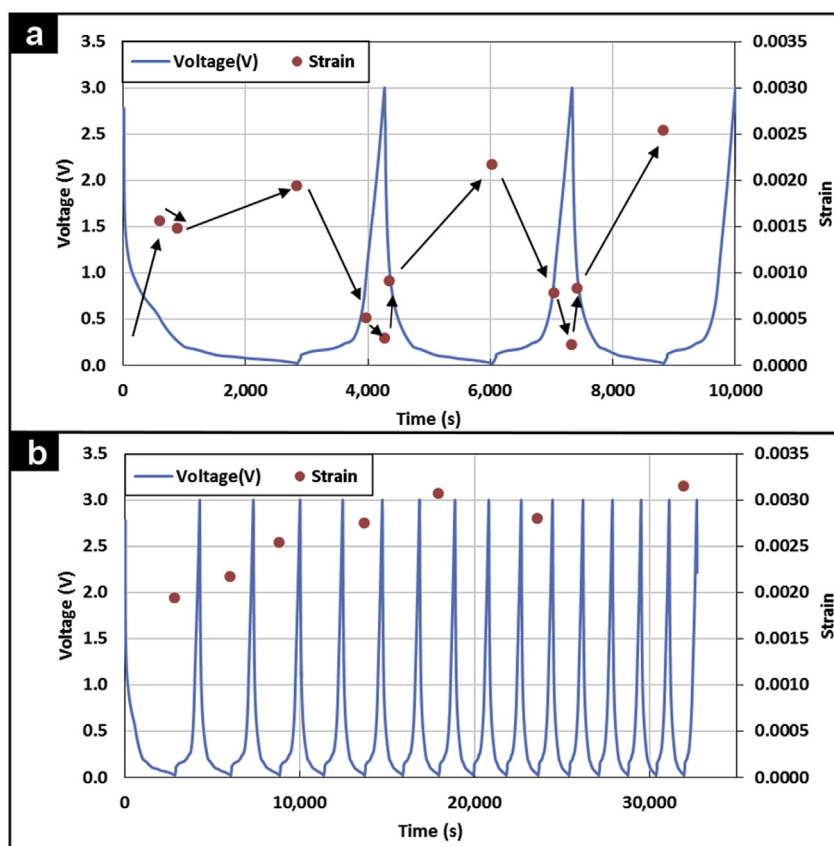

Fig. 4. For a graphite electrode with a copper foil substrate (16 μm), the electrical cycling and corresponding average electrode strains calculated via DIC at multiple points for the first few cycles (a) and at the maximum discharge state only (b).

An in-house written DIC algorithm was used to calculate the average bi-axial in-plane strain within the electrode films. Strains were computed in the plane of the electrode surface by differentiating the displacement fields found. These measurements were performed in both the vertical and horizontal directions (in the plane of the electrode film), and average strain values were calculated for the field of view region depicted in Fig. 3. Baseline measurements were used to quantify the noise in the measurements, with baseline displacement resolution for individual subsets determined to be approximately 1/10th of a pixel.

2.4. Battery geometry modeling

A model of the modified working-counter electrode battery geometry was meshed in ANSYS using PLANE121 elements, as shown in Fig. 3(a). An electrical potential field was then simulated between the top lithium counter electrode with the center through-hole and the full bottom working electrode using ANSYS. Center-holes of various diameters were simulated to determine the influence of removing of a portion of the lithium electrode. For each simulation, a uniform 3 V potential was applied between working electrode and counter electrode layer. The center-hole cases were compared to the potential distributions found for the "full" electrode (no center-hole) case.

3. Results and discussions

The results of ANSYS modeling for an electrical potential applied between the bottom working electrode and the top counter electrode with a center opening portion removed are shown in Fig. 3(b).

Of particular interest was the possible creation of electrical field gradients on the working electrode surface in the regions imaged in the experimental DIC analysis. On the working electrode surface, the only non-uniformities in the potential field found to exist were located beneath the inner edge of the counter electrode, Fig. 3(b). Otherwise, the center of the working electrode experiences a nearly uniform potential field.

The effects of the anode/cathode surface area ratio on electrochemical performance were also considered. Son et al., [35], examined these effects and found degraded coulombic efficiencies and discharge capacities for ratios greater than ~1.36. For this study, the same anode/cathode surface area ratio of ~1.13 was used for all specimens tested to minimize these effects. A number of control coin cell batteries without optical viewing windows (no holes in cap, separator, or cathode) were fabricated and electrically cycled. These control specimens exhibited very similar overall performance, including initial discharge capacity and capacity degradation, as the custom coin cell batteries.

The results of electrical cycling and the corresponding strains measured via DIC for graphite electrodes on foil and disk substrates are shown in Figs. 4 and 5, respectively. Average strains were found from differentiated displacement fields, and correspond to deformations that occurred with the imaged electrode surface with respect to the "as fabricated" state (assumed to be undeformed). This was confirmed by the strain gage characterization tests, which showed the residual strain level in all specimen types to be negligible (less than 0.014%). In both graphite cases, the maximum bi-axial tensile strains during each individual discharge/charge cycle were observed at the point of maximum discharge. For lithium battery, the maximum discharge point is physically related to the
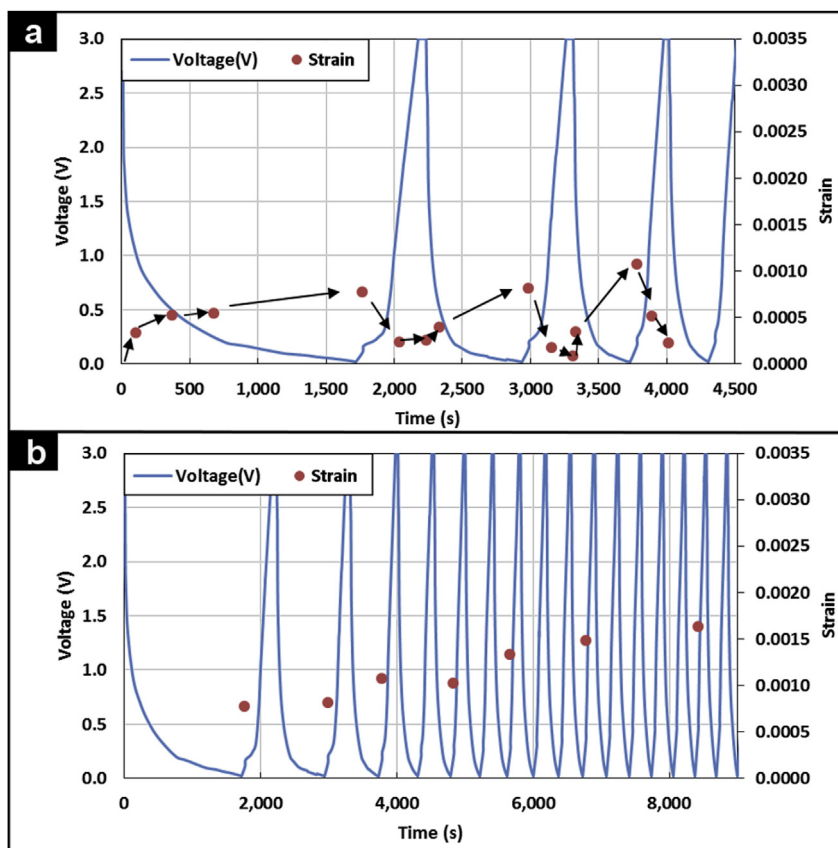

Fig. 5. For a graphite electrode with a copper disk substrate (635 μm), the electrical cycling and corresponding average electrode strains calculated via DIC at multiple points for the first few cycles (a) and at the maximum discharge state only (b).
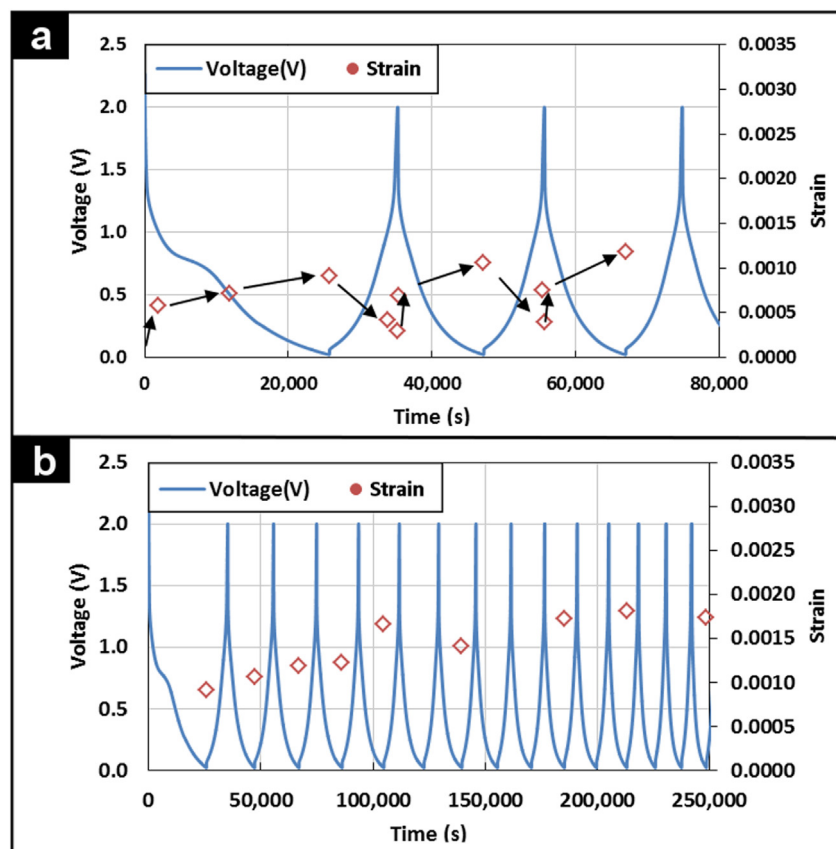
Fig. 6. For a CNT-based electrode with a copper foil substrate (16 μm), the electrical cycling and corresponding average electrode strains calculated via DIC at multiple points for the first few cycles (a) and at the maximum discharge state only (b).

state in which the graphite electrode is saturated with lithium ions. Similar behavior was observed in results for the CNT-based electrode specimens, shown for the foil case in Fig. 6 and the disk case in Fig. 7. The initial discharge capacities for all specimen types are shown in Table 1.

The strain magnitudes represent bi-axial in-plane deformations of the anode, which are greatly affected by the substrate constraint conditions. For both graphite and CNT-based electrodes, the strains within electrodes deposited on copper foil substrates were significantly larger than strains measured for the copper disk substrate specimens; an expected effect due to the greater rigidity of the disk. In all cases, out-of-plane deformations likely occur, but appeared to be uniform over the field of view based on focal plane observations. Though not directly measured, greater out-of-plane deformations likely occur for the disk substrate batteries to reach comparable volumetric expansions, and thus electrical capacities, as the foil cases.

One of the most significant observations is that as the number of discharge/charge cycles increases, there is a continual increase in the remnant strains within the working electrodes. In other words, to achieve the same potential charge at the end of each cycle, larger electrode deformations are required as the cycle number grows. At the same time, battery capacity decreases as the number of cycles increase. These effects are summarized for the graphite electrodes in Fig. 8, and for the CNT-based electrodes in Fig. 9. The results found in Figs. 8 and 9 are more similar than they might initially appear, and the differences that do exist can be attributed to a number of factors. One of the primary distinctions to note between the tests on the graphite and CNT cases is the high-end potential

used in each (3 V for the graphite electrodes, and 2 V for the CNT-based electrodes). As evidenced by Ref. [24], the discharge/voltage curve characteristics are vastly different for CNT and graphite electrodes.

In both CNT and graphite, the strains within the foil substrates are higher in magnitude as expected due to the greater substrate compliance. For the wider strain differential seen in the graphite electrode specimens, there was a wider differential in the discharge capacity. For the narrower strain differential found for the CNT-based electrodes, the discharge capacity curves are closer together. The narrower strain differential and lower overall strain magnitudes found for the CNT case can be attributed to the higher stiffness found for the CNT composite films (experimentally determined to be ~50–70 GPa, compared to ~10 GPa reported for graphite films).

In both types of electrodes, the rate of discharge capacity loss beyond 8 cycles is greater for the foil substrate specimens. The authors postulate that for the graphite films, the role of the substrate is to limit in-plane expansion. During Li intercalation, the entire film expands. Constraint from the substrate induces stresses and eventually cracking (similar to the case of thermal stresses that arise from constraint and thermal expansions not being allowed to occur). For the CNT-based films, expansion due to Li intercalation occurs at the individual fiber level with the binder matrix absorbing much of this deformation. In this case, the substrate acts to support the matrix and inhibit macroscale cracking.

The relationship between SEI formation and the induced graphite electrode strains was also explored through examination of the first electrical cycle, data for which is provided in
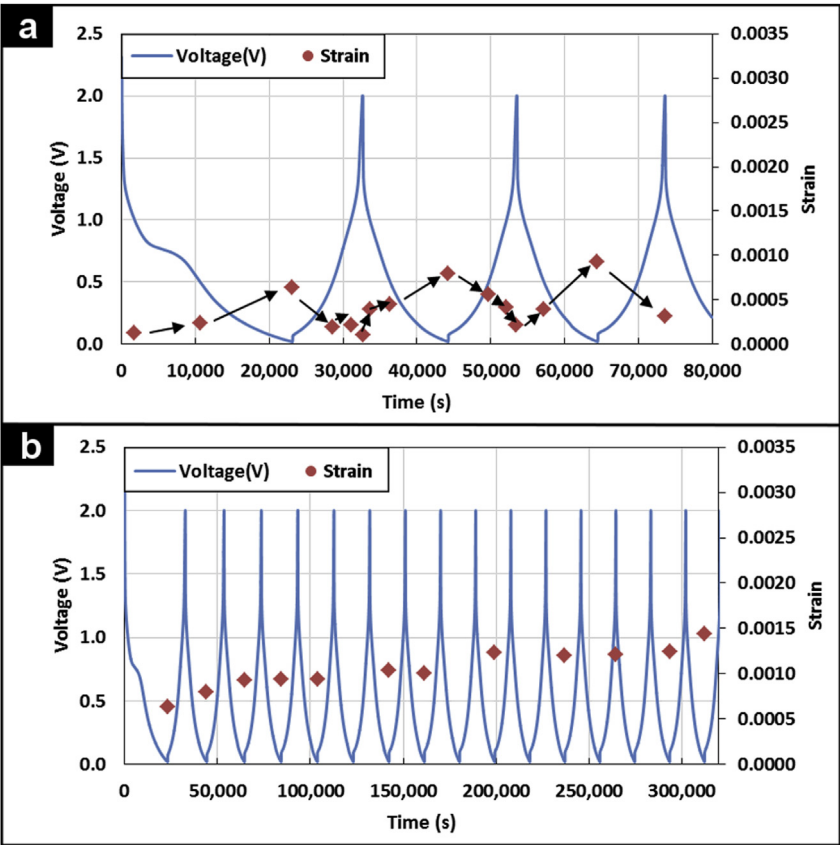
Fig. 7. For a CNT-based electrode with a copper disk substrate (635 μm), the electrical cycling and corresponding average electrode strains calculated via DIC at multiple points for the first few cycles (a) and at the maximum discharge state only (b).

Table 2. It is widely accepted that SEI formation occurs during the first electrical cycle and is responsible for much of the irreversible capacity loss found for nearly every type of commercially viable Li-ion battery configuration. Novak et al., [8] indicate that SEI formation occurs primarily in the 0.8 V–0.2 V regime during the first electrical cycle for graphite anodes. Over this potential range, SEI film formation did not appear to have a substantial mechanical effect. In fact, electrode strains due to Li-ion intercalation seem to occur throughout the entire discharge cycle.

4. Conclusions

During electrical cycling of custom lithium battery coin cells, quantitative *in situ* electrode deformations are reported showing the influence of substrate stiffness. Graphite electrode deposited on thin copper foil substrates showed over twice as much bi-axial strain was induced as that for comparable electrode deposited on thick copper disks electrically cycled under the same conditions.

Increasing electrode strains were found to be required to reach the same electrical charge state as the cycle number grew, which also corresponded with degraded discharge capacity. No significant mechanical electrode deformations were found to be associated specifically with SEI film formation during the initial electrical
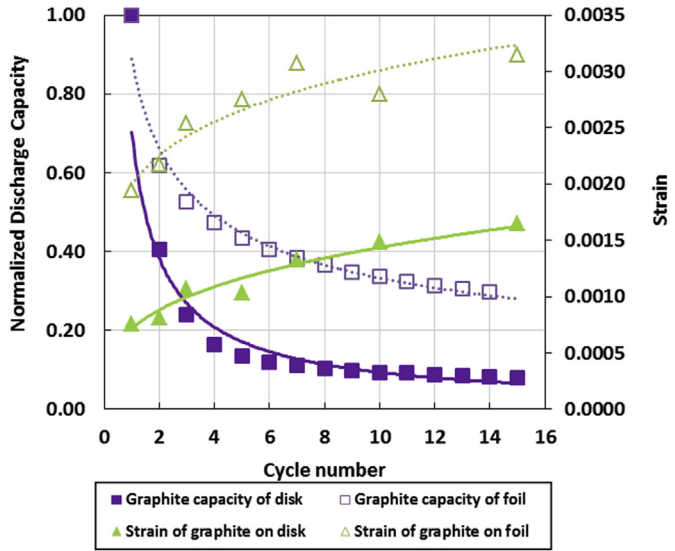

Fig. 8. Normalized discharge capacity and corresponding electrode strain for graphite electrode deposited on both copper foil and copper disk substrates are shown as the number of electrical charge/discharge cycles increases.
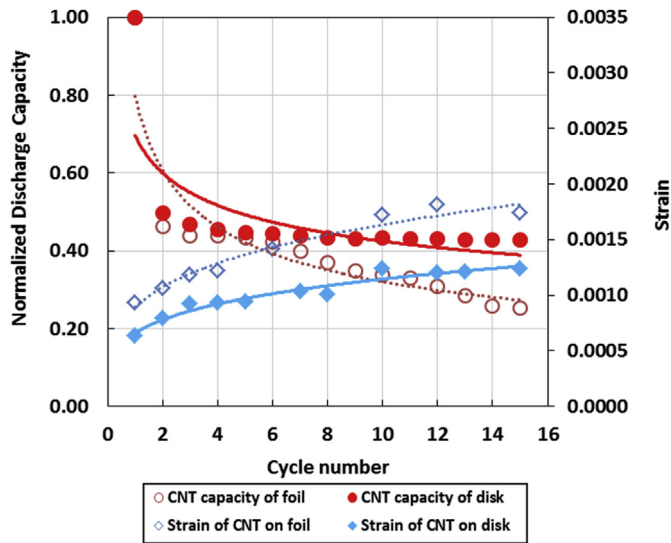
Table 1
Initial average discharge capacities.

Electrode type	Initial discharge capacity (mAh)	Electrode mass (mg)	Specific discharge capacity (mAh mg^{-1})
Graphite/Cu foil	0.728	3.80	192
Graphite/Cu disk	0.906	4.01	227
CNT/Cu foil	1.360	4.30	316
CNT/Cu disk	1.320	4.20	293

Fig. 9. Normalized discharge capacity and corresponding electrode strain for CNT-based electrode deposited on both copper foil and copper disk substrates are shown as the number of electrical charge/discharge cycles increases.

Table 2
Graphite electrodes, first cycle strains.

Electrode type	3.0 V–0.8 V Δ Strain (% of 1st cycle total)	0.8 V–0.2 V Δ Strain (% of 1st cycle total)	0.2 V–0.05 V Δ Strain (% of 1st cycle total)
Graphite/ Cu foil	0.00105 (54.1%)	0.000450 (23.2%)	0.000440 (22.7%)
Graphite/ Cu disk	0.000375 (48.4%)	0.000185 (23.9%)	0.000215 (27.7%)

cycle. Carbon nanotube-based electrode showed similar behavior, though at a reduced degradation rate.

References

[1] T. Nagaura, K. Tozawa, Prog. Batteries Sol. Cells 9 (1990).
[2] Y. Chang, H. Li, L. Wu, T. Lu, J. Power Sources 68 (1997) 187–190.
[3] F. Joho, B. Rykart, R. Imhof, P. Novák, M.E. Spahr, A. Monnier, J. Power Sources 81-82 (1999) 243–247.
[4] J. Shim, K.A. Striebel, J. Power Sources 119-121 (2003) 934–937.
[5] M. Winter, P. Novák, A. Monnier, J. Electrochem. Soc. 145 (1998) 428–436.
[6] F. Joho, B. Rykart, A. Blome, P. Novák, H. Wilhelm, M.E. Spahr, J. Power Sources 97-98 (2001) 78–82.
[7] V. Manev, I. Naidenov, B. Puresheva, G. Pistoia, J. Power Sources 57 (1995) 133–136.
[8] P. Novák, F. Joho, M. Lanz, B. Rykart, J.-C. Panitz, D. Alliata, R. Kötz, O. Haas, J. Power Sources 97-98 (2001) 39–46.
[9] W.-J. Zhang, J. Power Sources 196 (2011) 13–24.
[10] J. Li, A.K. Dozier, Y. Li, F. Yang, Y.-T. Cheng, J. Electrochem. Soc. 158 (2011) A689.
[11] J. Chen, S.J. Bull, S. Roy, H. Mukaibo, H. Nara, T. Momma, T. Osaka, Y. Shacham-Diamand, J. Phys. D. Appl. Phys. 41 (2008) 025302.
[12] P. Liu, N. Sridhar, Y.-W. Zhang, J. Appl. Phys. 112 (2012) 093507.
[13] Z. Ma, T. Li, Y.L. Huang, J. Liu, Y. Zhou, D. Xue, RSC Adv. 3 (2013) 7398.
[14] Y.H. Wang, Y. He, R.J. Xiao, H. Li, K.E. Aifantis, X.J. Huang, J. Power Sources 202 (2012) 236–245.
[15] F. Yang, J. Power Sources 196 (2011) 465–469.
[16] M.T. McDowell, S.W. Lee, W.D. Nix, Y. Cui, Adv. Mater. 25 (2013) 4966–4985.
[17] X.H. Liu, H. Zheng, L. Zhong, S. Huang, K. Karki, L.Q. Zhang, Y. Liu, A. Kushima, W.T. Liang, J.W. Wang, J.H. Cho, E. Epstein, S.A. Dayeh, S.T. Picraux, T. Zhu, J. Li, J.P. Sullivan, J. Cumings, C. Wang, S.X. Mao, Z.Z. Ye, S. Zhang, J.Y. Huang, Nano Lett. 11 (2011) 3312–3318.
[18] L.Q. Zhang, X.H. Liu, Y. Liu, S. Huang, T. Zhu, L. Gui, S.X. Mao, Z.Z. Ye, C.M. Wang, J.P. Sullivan, J.Y. Huang, ACS Nano 5 (2011) 4800–4809.
[19] L.-F. Cui, Y. Yang, C.-M. Hsu, Y. Cui, Nano Lett. 9 (2009) 3370–3374.
[20] T. Song, J. Xia, J.H. Lee, D.H. Lee, M.S. Kwon, J.M. Choi, J. Wu, S.K. Doo, H. Chang, W.I. Park, D.S. Zang, H. Kim, Y. Huang, K.C. Hwang, J.A. Rogers, U. Paik, Nano Lett. 10 (2010) 1710–1716.
[21] S. Kalnaus, K. Rhodes, C. Daniel, J. Power Sources 196 (2011) 8116–8124.
[22] I. Ryu, J.W. Choi, Y. Cui, W.D. Nix, J. Mech. Phys. Solids 59 (2011) 1717–1730.
[23] K. Zhao, M. Pharr, L. Hartle, J.J. Vlassak, Z. Suo, J. Power Sources 218 (2012) 6–14.
[24] C. de las Casas, W. Li, J. Power Sources 208 (2012) 74–85.
[25] J. Chen, Y. Liu, A.I. Minett, C. Lynam, J. Wang, G.G. Wallace, Chem. Mater. 19 (2007) 3595–3597.
[26] M. Jana, A. Sil, S. Ray, J. Phys. Chem. Solids 75 (2014) 60–67.
[27] L.-F. Cui, L. Hu, J.W. Choi, Y. Cui, ACS Nano 4 (2010) 3671–3678.
[28] V.A. Sethuraman, M.J. Chon, M. Shimshak, V. Srinivasan, P.R. Guduru, J. Power Sources 195 (2010) 5062–5066.
[29] V.A. Sethuraman, M.J. Chon, M. Shimshak, N. Van Winkle, P.R. Guduru, Electrochem. Commun. 12 (2010) 1614–1617.
[30] Y. Qi, S.J. Harris, J. Electrochem. Soc. 157 (2010) A741.
[31] E.M.C. Jones, M.N. Silberstein, S.R. White, N.R. Sottos, Exp. Mech. 54 (2014) 971–985.
[32] H.A. Bruck, S.R. McNeill, M.A. Sutton, W.H. Peters Iii, Exp. Mech. 29 (1989) 261–267.
[33] T.C. Chu, W.F. Ranson, M.A. Sutton, W.H. Peters, Exp. Mech. 25 (1985) 232–244.
[34] S.R. McNeill, W.H. Peters, M.A. Sutton, Eng. Fract. Mech. 28 (1987) 101–112.
[35] B. Son, M.-H. Ryou, J. Choi, S.-H. Kim, J.M. Ko, Y.M. Lee, J. Power Sources 243 (2013) 641–647.